

1 **Upper plate dynamic response to a sequential elastic rebound and slab acceleration**
2 **in laboratory-scale subduction megathrust**

3 **Ehsan Kosari^{1,2}, Matthias Rosenau¹, Thomas Ziegenhagen¹, and Onno Oncken^{1,2}**

4 ¹ Helmholtz Centre Potsdam, GFZ German Research Centre for Geosciences, Potsdam,
5 Germany.

6 ² Department of Earth Sciences, Freie Universität Berlin, Berlin, Germany.

7

8 Corresponding author: Ehsan Kosari (ehsan.kosari@gfz-potsdam.de)

9

10 **Key Points:**

- 11 • Analog megathrust earthquake experiments provide high-resolution observations to
12 evaluate the surface deformation signals from the shallow megathrust
- 13 • Surface displacement time-series suggest a sequential elastic rebound of the upper plate
14 and slab during great subduction megathrust earthquakes
- 15 • Dynamic slip reversal may be caused by rapid restoration of the upper plate after
16 dynamic overshooting and amplified upper plate motion
17

18 **Abstract**

19 An earthquake-induced stress drop on a megathrust instigates different responses on the upper
20 plate and slab. We mimic homogenous and heterogeneous megathrust interfaces at the laboratory
21 scale to monitor the strain relaxation on the two elastically bi-material plates by establishing analog
22 velocity weakening and neutral materials. A sequential elastic rebound follows the coseismic
23 shear-stress drop in our elastic-frictional models: a fast rebound of the upper plate and the delayed
24 and smaller rebound on the slab. A combination of the rebound of the slab and the rapid relaxation
25 (i.e., elastic restoration) of the upper plate after an elastic overshooting may accelerate the
26 relocking of the megathrust. This acceleration triggers/antedates the failure of a nearby asperity
27 and enhances the early slip reversal in the rupture area. Hence, the trench-normal rearward
28 displacement in the upper plate may reach a significant amount of the entire interseismic slip
29 reversal and speeds up the stress build-up on upper plate backthrust. Moreover, the backthrust
30 switches its kinematic mode from a normal to reverse mechanism reflecting the sense of shear on
31 the interface during coseismic and postseismic stages.

32

33 **Plain Language Summary**

34 Subduction zones, where one tectonic plate slides underneath the other, host the largest
35 earthquakes on earth. Two plates with different physical properties define the upper and lower
36 plates in the subduction zones. A frictional interaction at the interface between these plates
37 prevents them from sliding and builds up elastic strain energy until the stress exceeds their strength
38 and releases accumulated energy as an earthquake. The source of the earthquake is located
39 offshore; hence illuminating the plates' reactions to the earthquakes is not as straightforward as
40 the earthquakes occur inland. Here we mimic the subduction zone at the scale of an analog model
41 in the laboratory to generate analog earthquakes and carefully monitor our simplified model by
42 employing a high-resolution monitoring technique. We evaluate the models to examine the
43 feedback relationship between upper and lower plates during and shortly after the earthquakes. We
44 demonstrate that the plates respond differently and sequentially to the elastic strain release: a
45 seaward-rearward motion of the upper plate and an acceleration in the lower plate sliding
46 underneath the upper plate. Our results suggest that these responses may trigger another earthquake
47 in the nearby region and speed up the stress build-up on other faults.

48 **1 Introduction**

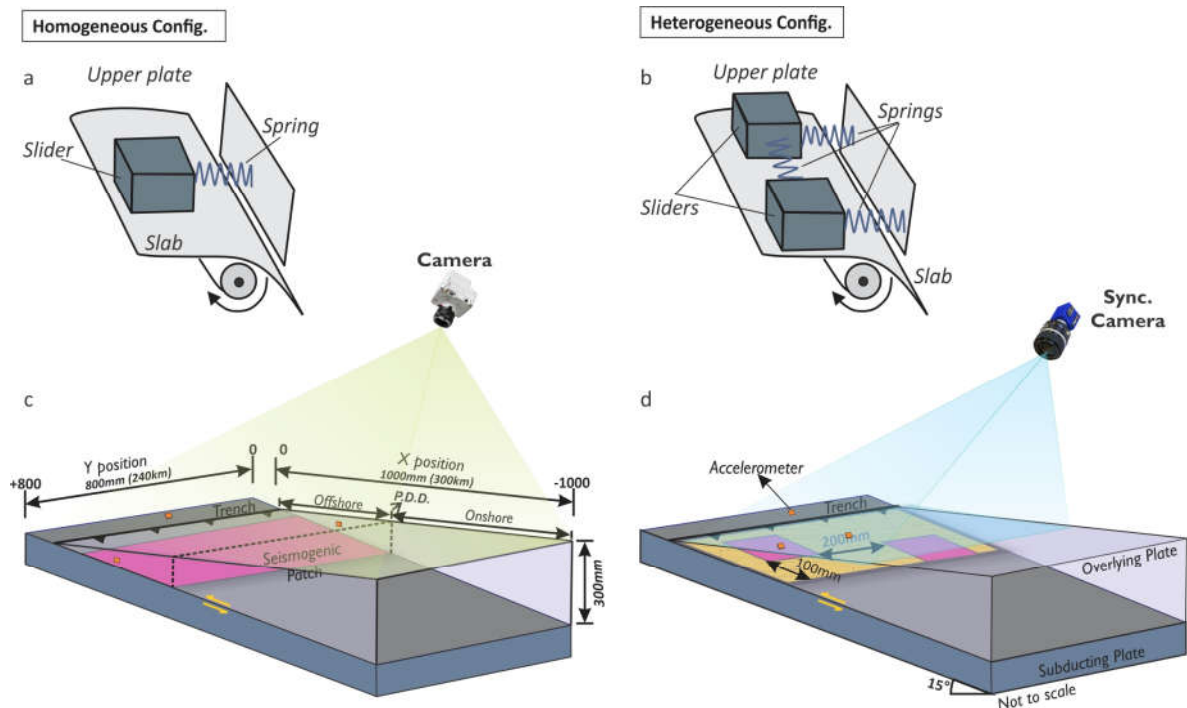
49 Large megathrust earthquakes (i.e., slip) cause a shear stress drop on the subduction interface that
50 drives the subduction system from a quasi-steady state interseismic loading stage (i.e., stick) to a
51 temporarily non-stationary (transient) relaxation mode. Although the static coseismic and
52 interseismic surface deformation of subduction megathrust has been analyzed in much detail (e.g.,
53 Chlieh et al., 2008; Loveless & Meade, 2011; Moreno et al., 2010; Schmalzle et al., 2014; Simons
54 et al., 2011), the dynamic motion of the upper plate caused by the transition from unstable (stable)
55 to stable (unstable) deformation has received somewhat less attention (Bedford et al., 2020). The
56 spatial and temporal resolution of the near-source observations is the main challenge of dynamic
57 instability analysis (Kosari et al., 2020). The transition from unstable to stable (i.e., postseismic
58 phase) involves different mechanisms over the shallow and deep parts of the subduction system,
59 which are rheologically dominated by elastoplastic (lithosphere) and viscoelastic (asthenosphere)
60 behavior, respectively (e.g., Wang *et al.*, 2012; Weiss *et al.*, 2019). To date, several postseismic
61 processes have been identified that can be seismic and aseismic, namely (1.) afterslip along the
62 megathrust (e.g., Hsu *et al.*, 2006; Bedford *et al.*, 2013; Hoffmann *et al.*, 2018), (2.) viscoelastic
63 relaxation of the lower crust and mantle of both slab and upper plate (e.g., Sun et al., 2014; Li et
64 al., 2015) and (3.) crustal faulting in the upper plate (extensional), accretionary wedge
65 (compressional), and shallow slab (extensional) (e.g., Kato et al., 2011; Hicks and Rietbrock.,
66 2015; Hoskins *et al.*, 2021). All these non-stationary mechanisms are triggered from stress drop
67 on the interface; hence, the stress drop pattern and magnitude and, on the other hand, the dynamics
68 of the slip are the main controlling factors.

69 Only a handful of megathrust earthquakes are relatively densely monitored. In many of these cases,
70 the early postseismic surface displacement above the ruptured asperity, which is remotely offshore,
71 exhibits intriguing signals that are interpreted differently (e.g., Bedford et al., 2016; Heki & Mitsui,
72 2013; Tomita et al., 2017; Watanabe et al., 2014). While the postseismic viscoelastic signal from
73 the relaxing asthenosphere appears with a characteristic long-term pattern and large-scale
74 wavelength (far-field, hundreds of kilometers scale) (e.g., Wang *et al.*, 2012; Sun and Wang,
75 2015), the postseismic elastic-frictional processes (i.e., relocking and afterslip) show relatively
76 steep gradients and short-wavelength (tens of kilometers scale) characteristics. These short-
77 wavelength postseismic signals, typically manifested in sustained seaward motion, interfere in the

78 near-field with the presumably steadier interseismic re-loading process that has a reverse kinematic
79 sense (i.e., landward motion in the upper plate). Such interference causes surface displacement
80 above the ruptured patch and nearby regions to be characterized by short time and short distance
81 changes in amplitude and direction, often causing local shear and vertical axis rotations. Such
82 "enigmatic patterns" are notoriously difficult to interpret, and discourse is rising about their
83 relevance for seismic hazard (e.g., Loveless, 2017; Melnick *et al.*, 2017; Yuzariyadi and Heki,
84 2021). Moreover, it is still not evident how the rupture propagation direction may cause these
85 enigmatic patterns. We here contribute to this discussion using observations and interpretations of
86 controlled analog megathrust experiments highlighting the potential variability of deformation
87 signals in subduction zones.

88 This study aims to address the sequential upper plate and slab elastic-frictional response during
89 the coseismic shear-stress drop and its early postseismic stage in a subduction megathrust system
90 by employing a series of carefully monitored analog modeling experiments. To examine the
91 feedback relationship between the upper plate and the slab, we investigate two generic
92 seismotectonic scale models representing seismically homogeneous and heterogenous subduction

93 megathrust systems and capture the model's surface displacements by employing a high resolution
 94 and high speed "laboratory seimogeodetic" method.



95

96

97 **Figure 1.** Scheme of the seismotectonic scale model's geometry and configuration: a and b demonstrate
 98 our conceptual systems of coupled spring sliders as depicted by Ruff and Tichelaar, (1996). b and c
 99 represent homogenous and heterogeneous configurations, respectively. The yellow (matrix) and magenta
 100 (main slip patch) rectangles demonstrate the seismogenic patches which generate repeating earthquake
 101 and megathrust events, respectively. P.D.D. represents the projection of the down-dip limit of the
 102 seismogenic patch on the model surface. The small orange rectangles show the different configurations of
 103 accelerometers. The frictional behavior of both velocity weakening materials used in the matrix and main
 104 slip patch has been visualized in Figure 2.

105 2 Methodology: Seismotectonic scale modeling

106 Seismotectonic scale models have been established to generate physically self-consistent analog
 107 megathrust earthquake ruptures and seismic cycles at the laboratory scale (Rosenau et al., 2009;
 108 2017, and references therein). They have been used to study the interplay between short-term

109 elastic (seismic) and long-term permanent deformation (Rosenau & Oncken, 2009), slip
110 variability (Rosenau et al., 2010), earthquake recurrence behavior and predictability (Corbi et al.,
111 2020; 2019; 2017; Rosenau et al., 2019), the linkage between offshore geodetic coverage and
112 coseismic slip model (Kosari et al., 2020) and to illuminate details of the seismic cycle (Caniven
113 & Dominguez, 2021). Analog models are downscaled from nature for the dimensions of mass,
114 length, and time to maintain geometric, kinematic, and dynamic similarity by applying a set of
115 dimensionless numbers (King Hubbert, 1937; Rosenau et al., 2009; 2017). The models generate a
116 sequence of tens to hundreds of analog megathrust earthquake cycles, allowing the analysis of the
117 corresponding surface displacement from dynamic coseismic (e.g., Movi S1) to quasi-static
118 interseismic stages.

119 2.1 Experimental setup and material behavior

120 2.1.1 Model scaling and similarity

121 The small-scale laboratory models should share geometric, kinematic, and dynamic similarities
122 with their prototype to be representative of a natural system as all lengths, time, and forces scale
123 down from the prototype in a consistent way dictated by scaling laws (King Hubbert, 1937).
124 According to Rosenau et al. (2009), we consider different timescales for coseismic and
125 interseismic deformation phases. They introduced a “dyadic” timescale that recognizes two
126 dynamically distinct regimes of the seismic cycle: the quasi-static interseismic regime, where
127 inertial effects are negligible due to the slow deformation rates, and the dynamic coseismic regime,
128 which is controlled by inertial effects. This allows us to slow down the earthquake rupture and
129 speed up the loading phase, keeping dynamic similarity in both stages (Table S1).

130 2.1.1.1 Interseismic phase scaling

131 In the quasi-static regime of the inter-seismic phase, scaling is identical to the common scaling of
132 long-term processes to the lab. For long-term tectonic studies involving materials that deform
133 brittle or viscous material, two dimensionless numbers, the Smoluchowski and Ramberg
134 (Ramberg, 1967) numbers, are of interest according to the deformation regime.

135 The Smoluchowski number is used to establish dynamic similarity in the case of brittle
136 deformation. This dimensionless number is defined as the ratio between overburden stress and
137 material strength.

138 *Equation 1:*

139
$$Sm = \frac{\rho g l}{C}$$

140 where ρ is density ($\text{kg}\cdot\text{m}^{-3}$), g gravitational acceleration (ms^{-2}), C cohesion (Pa), and l a
141 characteristic length.

142 According to the Smoluchowski number, cohesion should scale with density and length scale
143 following the scaling law:

144 *Equation 2:*

145
$$C^* = \rho^* L^*$$

146 where the asterisks represent the model / prototype ratios (i.e., $C^* = C \text{ model} / C \text{ prototype}$, $\rho^* = \rho$
147 $\text{model} / \rho \text{ prototype}$, $L^* = L \text{ model} / L \text{ prototype}$). All quantities with the stress unit (e.g., strengths)
148 and elastic moduli share the same scaling.

149

150 2.1.1.2 Coseismic phase scaling

151 For a short-term time (i.e., coseismic and postseismic stages), Froude scaling is used to reach
152 dynamic similarity (Rosenau et al., 2009):

153 *Equation 3:*

154
$$Fr = v / \sqrt{gl} = \text{inertia} / \text{gravitation}$$

155 while the timescale of the model should be the square root of the length scale:

156 *Equation 4:*

157
$$T^* = \sqrt{L^*}$$

158 Note that all accelerations are the same in the model as in the prototype. The Cauchy number can
159 be used for reaching the stress scale in the dynamic regime (Rosenau et al., 2009):

160 *Equation 5:*

161
$$Ca = \rho v^2 / B = \text{inertia} / \text{elasticity}$$

162 where B is an elastic modulus.

163 The model parameters without a dimension should be the preserved Poisson's ratio ν , the friction
164 coefficient, and the friction rate and state parameters. An exception to this general scale in-
165 dependence of dimensionless parameters is the moment magnitude M_w that is related to the
166 seismic moment (unit Nm) but defined as being dimensionless:

167 *Equation 6:*

168
$$M_w = 2/3 \log_{10} (M_0) - 10.7$$

169 Here I scale up analog earthquake moment magnitude non-linearly by applying the scale factor of
170 seismic moment M_0^* :

171 *Equation 7:*

$$172 \quad M^{\text{prototype}}_w = M^{\text{model}}_w - 2/3 \log M_0^*$$

173 Typically, magnitudes of analog earthquakes are in the range of -6 to -7 , which correspond to
174 earthquakes of $M_w = 8-9$ in nature.

175

176 2.1.2 Model geometry and configuration

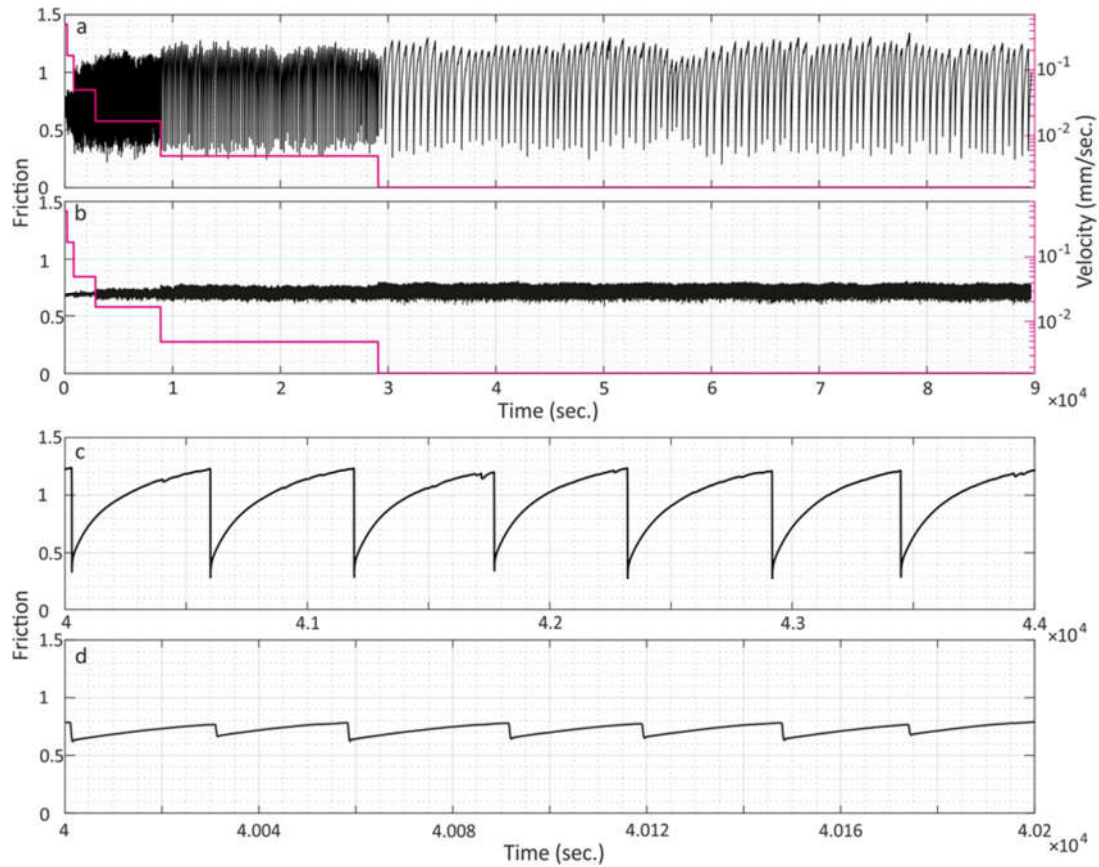
177 In the presented 3-D experimental setup modified from Rosenau *et al.* (2019) and introduced in
178 Kosari *et al.* (2020), an ocean-continent subduction forearc model is set up in a glass-sided box
179 (1,000 mm across strike, 800 mm along strike, and maximal 300 mm deep) with a 15° dipping,
180 elastic basal rubber conveyor belt (the model slab), and a rigid backwall. A flat-topped wedge
181 made of an elastoplastic sand-rubber mixture (50 vol.% quartz sand G12: 50 vol.% EPDM-rubber)
182 is sieved into the setup representing a 240 km long forearc segment from the trench to the volcanic
183 arc (Figures 1).

184 At the base of the wedge, zones of velocity weakening controlled by granular stick-slip (“seismic”
185 behavior) are realized by emplacing compartments of either sticky-rice (“main slip patches”) or
186 fine-grained salt (“matrix”), which generate quasi-periodic large and small slip instabilities,
187 respectively (Figures 1), mimicking megathrust earthquakes of different size and frequency. Large
188 stick-slip instabilities in the main slip patch(es) (MSP) are almost complete and recur at low
189 frequency (~ 0.2 Hz), while those in the matrix are partial ($< 10\%$) and at high frequency (~ 10 Hz)
190 at a prescribed constant convergence rate of $50 \mu\text{m/s}$. This bimodal behavior is intended to mimic
191 rare great (M8-9) earthquakes versus small frequent repeating events (e.g., Uchida and Bürgmann,
192 2019; Chaves *et al.*, 2020) in a creeping environment akin to established concepts of the shallow
193 subduction megathrust (e.g., Bilek and Lay, 2002). The wedge itself and the conveyer belt respond
194 elastically to these basal slip events similar to crustal rebound during natural subduction
195 megathrust earthquakes. Upper plate faults (in our case, a single backthrust fault) gradually emerge
196 self-consistently downdip and up-dip of the main slip patches and accommodate plastic upper plate

197 shortening over seismic cycles, as documented in earlier studies (Kosari et al., 2020; Rosenau et
198 al., 2009, 2010; Rosenau & Oncken, 2009).

199 Two different seismic configurations of the shallow part of the wedge base (the megathrust)
200 represent the depth extent of the seismogenic zone in nature. In the first configuration, hereafter
201 named “homogeneous configuration”, a single large rectangular stick-slip patch
202 (Width*Length=200*800 mm) is implemented as the main slip patch (MSP). This setup represents
203 a system of a homogeneous seismogenic zone with temperature-controlled depth range and no
204 variation along strike generating M9 type megathrust events similar to the 2004 Sumatra
205 earthquake (Ammon et al., 2005; Lay et al., 2005). In the second case, hereafter named
206 “heterogeneous configuration”, two square-shaped MSPs (200*200mm) have been emplaced,
207 acting as two medium-size seismogenic asperities generating M8-9 type events similar to, for
208 example, the 2010 Maule (Chile) earthquake (Moreno et al., 2010). These two patches are at a
209 center-to-center distance of 400mm and 100mm in trench-parallel and trench-normal direction,
210 respectively, while they are surrounded by a salt matrix hosting frequent small events (Figures 2).
211 For minimizing boundary conditions, these MSPs are placed at a reasonable distance from the
212 sidewalls. Backthrusts accommodating long-term permanent wedge shortening and uplift emerge
213 in the upper plate in both configurations during the model evolution. They are rooted in the down-
214 dip limit of the stick-slip patch(es), where compressive stresses peak along the plate interface

215 during the interseismic period. Because this backthrust shows normal faulting mechanism during
216 the coseismic stage, we term this fault “antithetic fault”.



217

218 **Figure 2.** Friction drop time-series measured during velocity stepping tests under constant normal load
219 simulating coseismic and interseismic friction drop and increase. The periodic friction drops represent
220 analog earthquakes. a and c (main slip patch in Figure 1) and magenta (matrix in Figure 1) demonstrate
221 the seismogenic patches which generate megathrust events and repeating earthquakes, respectively. c and

222 *d show seven seismic cycles from both materials. Note that the recurrence of the repeating earthquake is*
223 *approximately 20 times shorter than the megathrust event.*

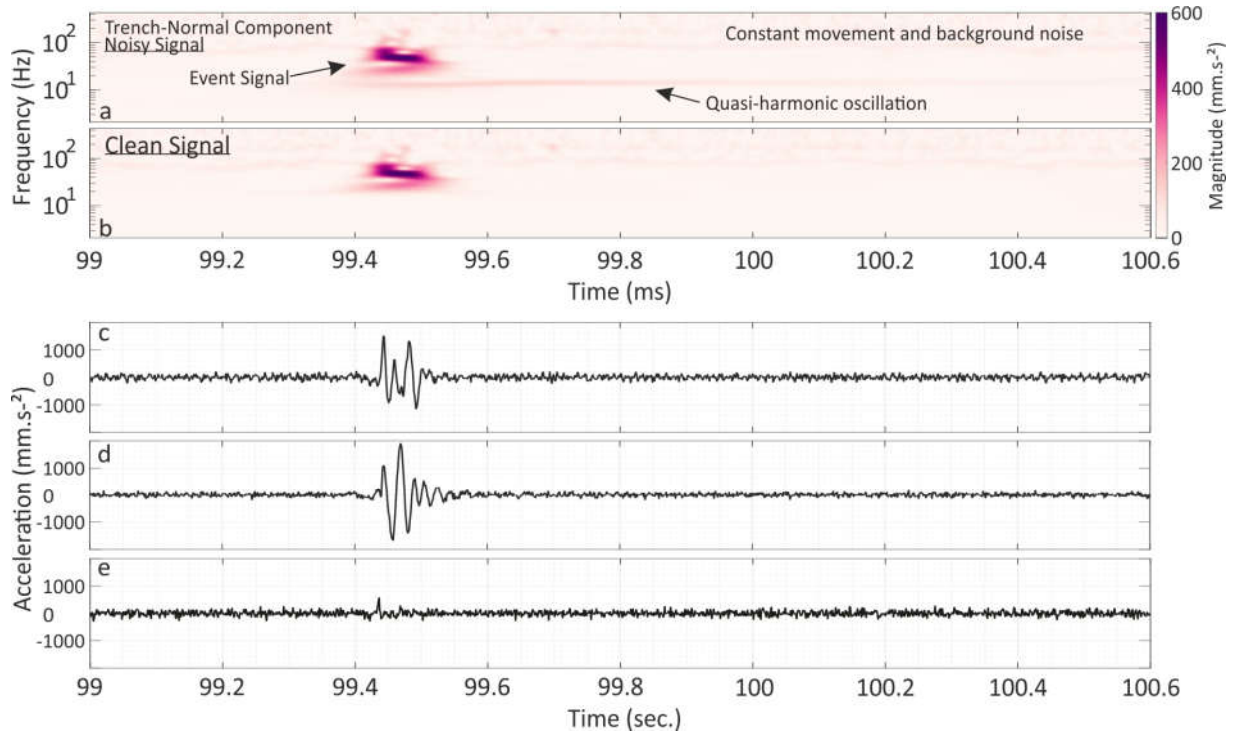
224 2.2 Experimental monitoring: Laboratory seismogeodesy

225 A combination of seismological and geodetic methods applied to laboratory-scale models allows
226 us to monitor the model's deformation at high spatial and temporal resolution and derive
227 observational data equivalent to natural observations.

228 2.2.1 Laboratory geodesy

229 To capture horizontal micrometer-scale surface displacements associated with analog earthquakes
230 at microsecond scale periods, we monitor the model surface with a highspeed CMOS
231 (Complementary Metal Oxide Semiconductor) camera (Phantom VEO 640L camera, 12 bit, 4
232 MPx) intermittently at 250 Hz (Figure 1). A complimentary high-speed camera (200 Hz) is added
233 to the monitoring system for synchronizing with the accelerometer. This synchronization allows
234 differentiating the potential quasi-harmonic oscillations caused by dynamic frictional instability
235 (i.e., coseismic) from event signals. Digital image correlation (e.g., Adam et al., 2005) has been
236 applied at high spatial resolution (~ 0.02 mm) via the DAVIS 10 software (LaVision GmbH,
237 Göttingen/DE). Data are processed to yield observational data similar to those from an ideal dense
238 and full coverage (on- and offshore) geodetic network, that is, velocities (or incremental
239 displacements) at locations on the model surface. We use an analog geodetic slip inversion
240 technique (AGSIT, Kosari et al., 2020) to invert surface displacements for model megathrust slip
241 and backslip distribution over earthquake cycles. Note that although all observations can be

242 upscaled to nature using scaling laws (King Hubbert, 1937; Rosenau et al., 2009, 2017), we here
243 report all values at the laboratory scale.



244
245 **Figure 3.** Differentiating Quasi-harmonic oscillation and event-related signal. *a* and *b* represent the
246 scalogram of the signal before and after filtering the quasi-harmonic oscillations out. *c* and *d* are the
247 normal-trench acceleration derived from three sensors located on the wedge (*c* and *d*) and the basal rubber
248 conveyor belt (*e*).

249 2.2.2 Laboratory seismology

250 The experiments are additionally monitored using triaxial capacitive accelerometers (MEMS:
251 micro electromechanical systems). The sensors can measure with a sampling frequency of 10 kHz
252 and a measuring range from 0 to ± 2 g. The bandwidth of the sensors depends on the sensor type
253 and axis, ranging from 500 Hz to 1500 Hz. We established three sensors positioning in different

254 configurations to cover any possible motion in the setup, from the coseismic surface motions to
255 the harmonic oscillations. The sensors run at 1 kHz to avoid the aliasing effect.

256 **3 Results: Observations and interpretations**

257 In the following, we analyze high-resolution time-series of surface and slab displacements and slip
258 along the megathrust and an emergent upper plate fault over several seismic cycles. We analyze
259 the heterogeneous model in-depth (compared to the homogeneous configuration) to capture the
260 details of upper plate and slab responses in the coseismic and early-postseismic stages (Figures 4
261 & 6). We consider the Coulomb Failure Stress Change (ΔCFS) over coseismic and early-
262 postseismic stages and its impact on model slab velocity changes (Figures 5). Subsequently, we
263 evaluate the elastic rebound of the slab and the upper plate in response to the mainshock-induced
264 stress changes. Finally, we explore the combined effect of the stress changes and elastic rebounds
265 on the accumulation of the horizontal displacement in the upper plate and earthquake triggering
266 (Figure 10).

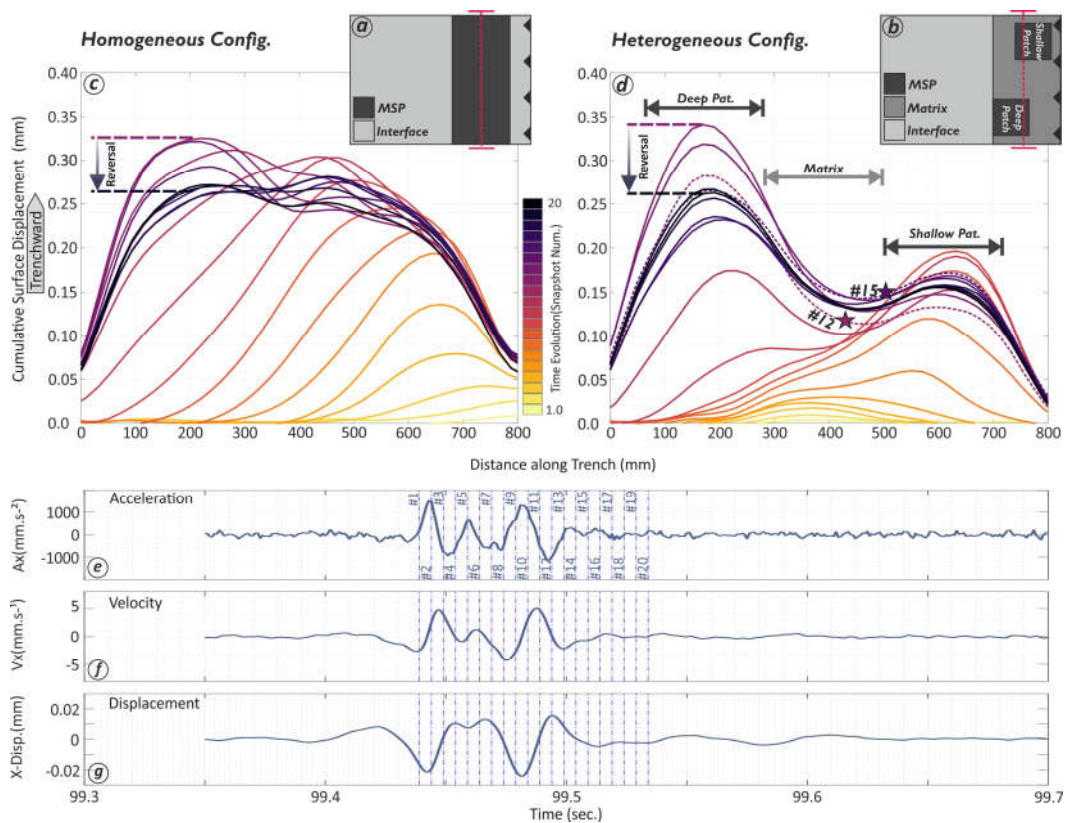
267 3.1 Kinematic observations and interpretations

268 3.1.1 Time-variable surface displacements and slip over an analog earthquake and the 269 early postseismic

270 As the recorded signals may occur at different scales, the scalogram of the synchronized
271 accelerometer has been used to differentiate coseismic surface displacement versus machine-
272 related oscillation and quasi-harmonic oscillations caused by dynamic frictional instability (Figure
273 2). The scalogram shows the absolute value of the waveforms, plotted as a function of time and
274 frequency. The high-frequency signals (>60 Hz) include the constant vibration of the machine and
275 background noise. The slip event's elastic wave frequency ranges from 20 to 60 Hz, and the lower
276 values (<20 Hz) represent the event-triggered quasi-harmonic oscillations while it can also be
277 tracked on the model's sidewalls after each event. The oscillation is removed from the signals
278 using a highpass filter. The timing of each snapshot from the synchronized camera is marked on

279 the cleaned waveform to disregard the oscillation, and accordingly, 20 snapshots are selected to
 280 cover the coseismic and early-postseismic stages.

281 Figures 4c and d visualize the cumulative surface displacements averaged over the area above the
 282 seismogenic zone along the strike of the megathrust for both configurations (see Figures S1 & S2
 283 for 2D surface displacement map). Figure 5a-b shows corresponding snapshots of the inverted slip
 284 along the megathrust and upper plate fault (antithetic to the megathrust) inverted from surface



285

286 **Figure 4.** Model setup and exemplary evolution of coseismic and early-postseismic surface deformation in
 287 two scenarios. a and b: Plan view of the seismotectonic scale models' configurations; Light, medium, and
 288 dark gray colors represent the velocity neutral ("aseismically" creeping) interface, a velocity weakening
 289 matrix characterized by microslips ("microseismicity"), and the main slip patch(es) (MSP) where large
 290 analog megathrust earthquake slip occurs ("seismogenic zone" or "asperity"), respectively. The red
 291 dashed lines show the profiles along which the cumulative surface displacement is shown in c and d. The
 292 downward vectors indicate surface displacement reversal during the early-postseismic stage interpreted as
 293 backslip. The corresponding surface deformation maps derived from the synchronized camera are
 294 visualized in figures S1 and S2. The stars on the dashed lines show the selected surface displacement

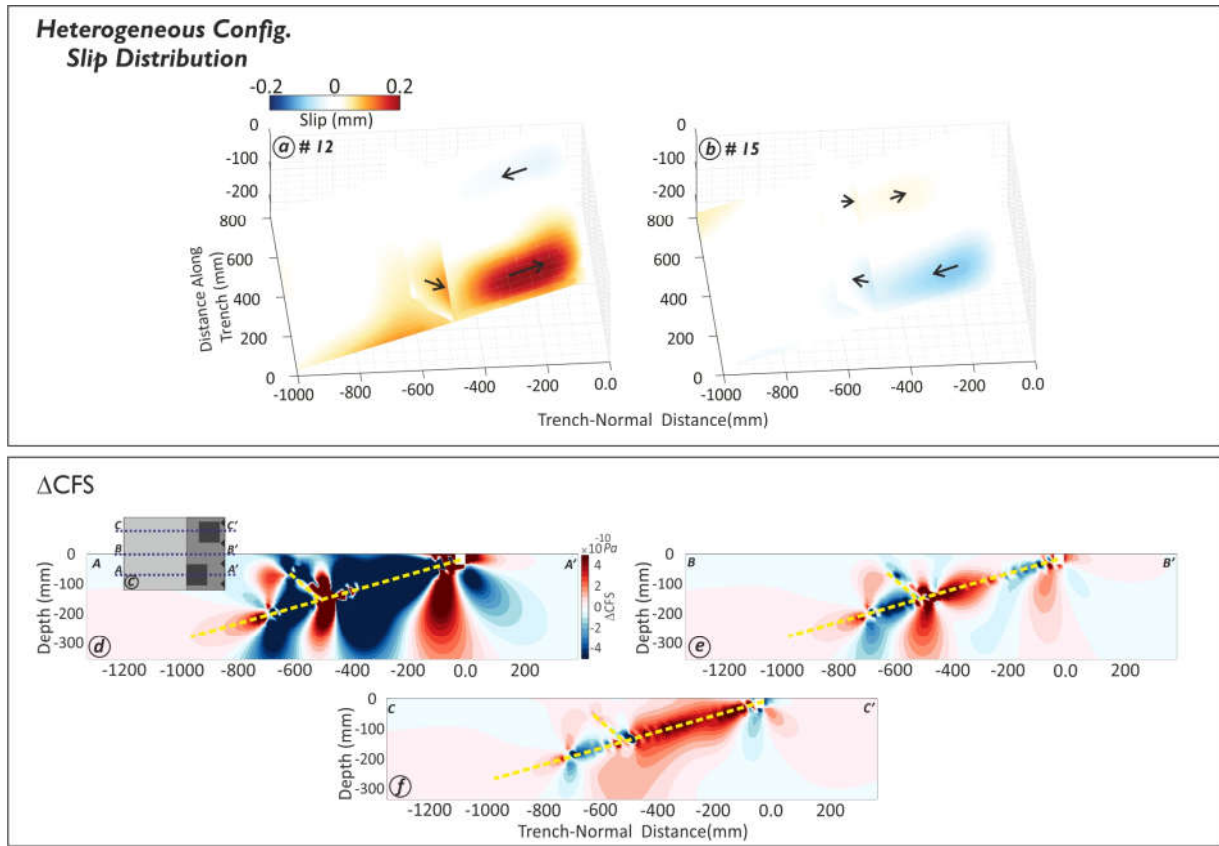
295 *snapshots for slip modeling in Figure 5. e-g show an exemplary acceleration, velocity, and displacement*
296 *of the one sensor located on the wedge (Figure 2c). The timing of each snapshot has been marked on the*
297 *waveforms.*

298 displacements. In the homogeneous system, the rupture initiates at the periphery of the stick-slip
299 zone, grows radially in a crack-like fashion, and then laterally propagates as a pulse across it
300 (Figures 4c and S1). While the rupture arrests on the opposite side, the early rupture area seems to
301 have relocked and apparently accumulates backslip at an even higher rate than the plate
302 convergence rate. We term this kinematic observation “postseismic slip reversal” as it appears as
303 a normal faulting mechanism in its formal inversion. However, the observation could also be
304 explained by locking of the interface (no slip) combined with transient slab acceleration. Whatever
305 the source, the slip reversal is short-lived and propagates along the interface as the pulse behind
306 the rupture. At the surface, this early instantaneous backslip (slip reversal) on the megathrust
307 reduces the cumulative trenchward surface displacement (Figure 3c). The lack of significant
308 afterslip in the MSPs and the matrix immediately after the coseismic stage and the rearward surface
309 displacement of the upper plate suggests a nearly complete stress-drop allowing the MSP and
310 matrix to enter the relocking phase.

311 In the heterogeneous system, the rupture nucleates in the matrix, where a small foreshock event
312 first triggers the failure of the shallow patch followed by failure of the deeper patch (Figures 4d
313 and S2). Because of the limited along-strike dimension of the MSP, megathrust failure occurs as a
314 sequence of two discontinuous crack-like failures in contrast to the more continuous pulse-like
315 failure in the uniform model. Again, a postseismic slip reversal occurs in the shallow MSP while
316 the deep MSP is still in the process of failing (Figure 5a) and where slip reversal occurs slightly
317 later. The rearward displacement of the upper plate predominantly occurs above the site of the two
318 moderate-size MSPs. In other words, the MSPs, which host large slips, undergo larger postseismic
319 slip reversal than the matrix.

320 3.1.2 Upper plate displacement accumulation

321 In both configurations, the postseismic backslip initiates immediately following the main event on
322 the patches. The maximum amount of the backslip-caused surface displacement could reach 30%
323 of the maximum coseismic surface displacement. The trench-normal surface displacements of the



324

325 **Figure 5.** Upper panel: Slip models of the selected increments (marked in Figure 1d) in the
 326 heterogeneous system for demonstrating slip/backslip distribution in the MSPs and the antithetic
 327 upper plate fault. The vectors indicate the relative sense of slip but are not to scale. The lower
 328 panel represents three trench-normal profiles of Coulomb failure stress changes (ΔCFS) from the
 329 slip model snapshot #12 in the heterogeneous configuration. Inset shows the location of profiles
 330 on the model surface.

331

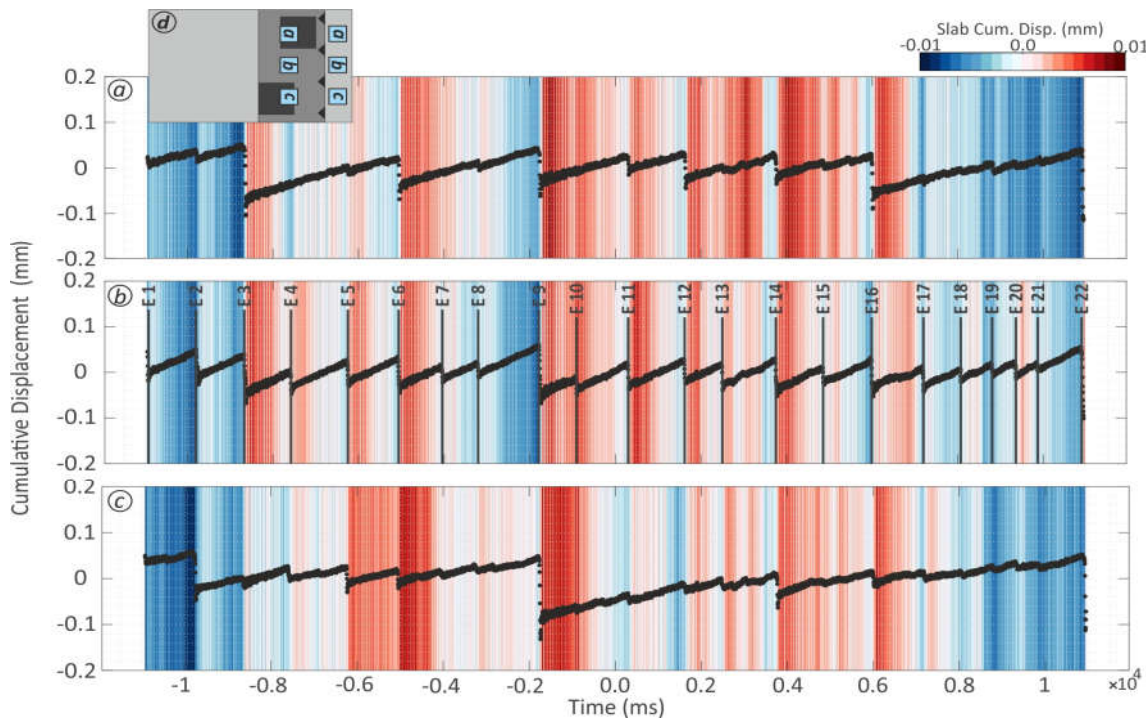
332

333 coseismic, postseismic, and interseismic stages of an earthquake cycle have been visualized in
 334 Figure S5. Comparing the magnitude of the cumulative surface velocities reveals that the
 335 horizontal surface displacement (mostly seafloor in nature) during the early parts of the
 336 postseismic stage could reach up to 20-30% of the entire interseismic backslip.

337 In the upper plate, we observe a synthetic and kinematically consistent reactivation of the
 338 backthrust, i.e. as a normal fault during the coseismic megathrust slip phase and as a thrust in

339 response to backslip on the megathrust. A slip (‘trenchward’) or backslip rearward (‘landward’)
 340 on the interface may re-activate the antithetic fault in the upper plate with a normal (e.g., #12 in
 341 Figure 5a) and/or a reverse sense of movement (e.g., #15 in Figure 5b), respectively. Following
 342 the slip distribution model (Figure 5a & b), two segments of the upper plate fault may move in
 343 opposite directions. This behavior likely reflects the shear sense on the MSPs. Particularly, in the
 344 upper plate fault, which in our experiments is rooted in the plate interface at the down-dip end of
 345 the seismogenic zone, the sense of slip (slip/backslip) on the seismogenic zone directly controls
 346 the slip mechanism of the antithetic fault.

347 Based on the antisymmetric part of the two-dimensional velocity gradient tensor, we calculate the
 348 vertical axis rotation of the upper plate (Figure 8, the methodology can be found in Allmendinger
 349 et al., 2007). The uniform and dense distribution of the observation points at the model surface
 350 allows us to use the nearest neighbor points to calculate each point's rotation around a vertical axis.
 351 In the case of coseismic trenchward displacement of the upper plate, a divergent motion in the
 352 surface velocities above the rupture zone leads to a (sub-) symmetric vertical rotation while it may
 353 also rotate the adjacent areas. However, there is no significant rotation above the nearby (deeper)
 354 asperity. On the other hand, in the stage that two MSPs are on opposite modes (loading vs.
 355 unloading), the surface velocities above the loading MSP show a convergence mode as it may
 356 enhance the shortening rate in the early postseismic stage.

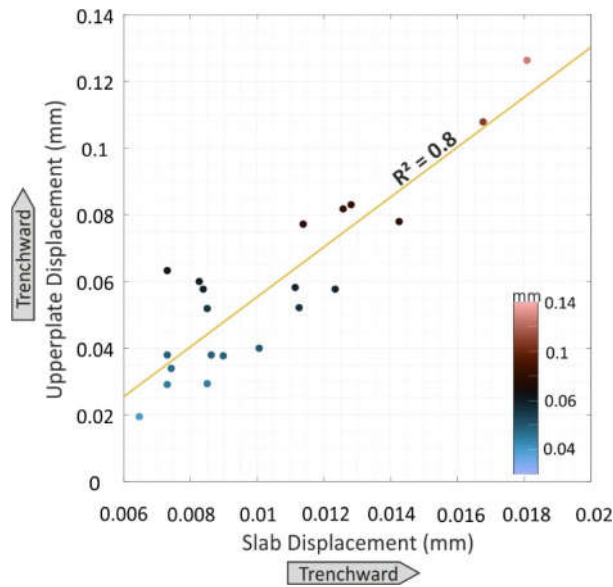


358 **Figure 6.** *Upper plate time-series overlaid on the slab time-series (background colormap) from*
359 *the heterogeneous configuration (see Figure S4 for the homogenous configuration). Note the*
360 *location of the profiles relative to the upper plate and slab. The vertical lines (E1-E22) indicate*
361 *abrupt surface displacement changes above the matrix. The warm color shows the landward*
362 *displacement of the slab. Larger events instigate greater slab responses (Figure 7).*

363

364 3.2 Dynamic interpretations: Coulomb failure stress changes

365 To constrain the triggering dynamics, we consider static stress changes in our models. Based on
366 the slip and backslip pattern documented above, we derive Coulomb failure stress changes (ΔCFS)
367 (e.g., Lin and Stein, 2004) induced by the mainshock on the megathrust and the antithetic fault to
368 get insight into zones of enhanced/decreased CFS (lower panel in Figure 5 and S3). We calculate
369 the ΔCFS for the coseismic and postseismic stages of an event for the heterogeneous system on
370 the receiver faults with the same sense and orientation as slip (thrust receiver faults in Figure 5)
371 and backslip (normal receiver faults Figure S4) on the interface. In the shallow part of the plate
372 interface (profile c-c'), a negative ΔCFS lobe is bounded by two positive ΔCFS lobes. The ΔCFS
373 is highly enhanced at the upper limit of the rupture, where the shallow part of the interface ruptures
374 and is adjacent to the main slip zone on the slab. The ΔCFS on the normal receiver fault (Figure
375 S3) shows a decrease and an increase at the up-dip limit of the deep (in slip phase) and shallow (in
376 backslip phase) MSPs on the slab, receptively.



377

378 **Figure 7.** Correlation between the upper plate and slab trenchward (landward) displacements
 379 during coseismic and early-postseismic stages.

380

381 Another lobe of positive Δ CFS is extended to the down-dip limit of the main rupture area, where
 382 the antithetic fault in the upper plate appears during the model evolution (Figure 5). The deep-
 383 rooted antithetic fault, which imposes a significant discontinuity in the upper plate, perturbs the
 384 inner-wedge stress state and highly increases the CFS at the conjunction of the interface and the
 385 antithetic fault. Hence, it builds up stress and enhances the Δ CFS in the upper plate. However, the
 386 uncertainties in the slip distribution models at the conjugation zone may affect the Δ CFS's
 387 uncertainty. A relatively strong increase in CFS is predicted for the deeper MSP. Likely, it results
 388 from a combination of backslip on the deeper MSP and the mainshock-induced stress transfer.

389

390 **4 Discussion and conclusion**

391 4.1 Inertia-dominated instability

392 The behavior of frictional properties is commonly defined in the framework of rate-and-state
 393 friction (RSF). The rate-and-state friction law can lead to stable (a - b) > 0 or unstable slip (a - b)
 394 < 0 depending on the friction parameters (Rice, 1993; Rice & Ruina, 1983):

395 Equation 8:

396

397

$$\mu(V, \theta) = \mu^* + a \ln\left(\frac{V}{V^*}\right) + b \ln\left(\frac{V^* \theta}{Dc}\right)$$

398

399

400

401

402

403

404

405

406

407

408

where μ^* is the coefficient of friction measured at sliding velocity V^* . The parameters a and b represent the frictional properties of the material. The parameter $(a - b)$ represents the velocity-dependence of μ at steady-state, with positive values (i.e., $a > b$) resulting in velocity-strengthening and negative values resulting in velocity-weakening behavior (seismogenic zone). Rice and Tse (1986) propose an inertial scale set and a state relaxation scale in a single degree of freedom elastic system in frictional constitutive models. They suggest that once inertia exerts its control of acceleration while the slip velocity is very high, the state relaxation can be neglected. In other words, during high slip motion in unstable phase ($a-b < 0$), full dynamic effects have to be considered as the slip stages, including acceleration, deceleration, and arrest, that are all controlled by inertia:

Equation 9:

409

$$(T/2\pi)^2 \frac{d^2\delta}{dt^2} = (\delta_0 - \delta) - \tau/k$$

410

411

412

413

414

415

416

where $T/2\pi$ is inertia time (characteristic vibrational time), δ_0 and δ represent distances, and τ and k show frictional stress and stiffness.

Rice and Ruina (1983) show that sliding at the velocity V_l can be stable only when the system stiffness (K) is larger than the critical stiffness (K_c):

Equation 10:

415

416

$$K_c = \frac{(b - a)\sigma'}{D_c} \left[1 + \frac{MV_l^2}{\sigma' a D_c} \right]$$

417

418

419

420

421

422

423

The critical stiffness is written as the sum of a quasi-static critical stiffness ($K_{c,qs}$) and a dynamic critical stiffness ($K_{c,dyn}$) as the first term shows a quasi-static critical stiffness, and the second term is a dimensionless number representing the dynamic effect. The transition from a quasi-static stick-slip to a harmonic oscillation can be described by the emergence of the dynamic instability coefficient η (Im et al., 2019; Im & Avouac, 2021):

Equation 11:

$$\eta = \frac{MV_l^2}{\sigma' a D_c}$$

424

425 This parameter shows that the system tends to become unstable for a larger mass or velocity and
426 is sensitive to the loading velocity ($\eta \sim V_l^2$) representing the contribution of inertia to frictional
427 instability (Im & Avouac, 2021). In the case of a single-degree-of-freedom spring and slider
428 system, the inertial vibration tends to emerge when $\eta > 1$ (Im et al., 2019). In the cases that the
429 inertial instability, MV_l^2 , is high or normal stress is low, friction-induced vibration (harmonic
430 oscillation) may appear in any system exhibiting velocity weakening friction ($a - b < 0$).

431 Comparable with nature, the normal load in the shallow part of the subduction megathrust (i.e.,
432 the offshore portion in nature) is sufficiently low (Gao & Wang, 2017) and does not change during
433 the coseismic period considerably. However, loading velocity increases significantly. These
434 normal stress and velocity conditions prompt the system, which is already in unstable mode
435 (i.e. slip; $a - b < 0$), to the $\eta > 1$ domain (Figure 1 in Im and Avouac., 2021) and lead to an inertia-
436 dominated instability appearing as a harmonic oscillation in our elastoplastic wedge (i.e., upper
437 plate). This inertia-dominated instability is evident with the onset of the megathrust event (Figure
438 3) and may enhance the slip/backslip on the interface, similar to the effect of “dynamic shaking”
439 on the plate interface coupling in Southern Cascadia (Materna et al., 2019).

440 4.2 Sequential elastic rebound of upper plate and slab?

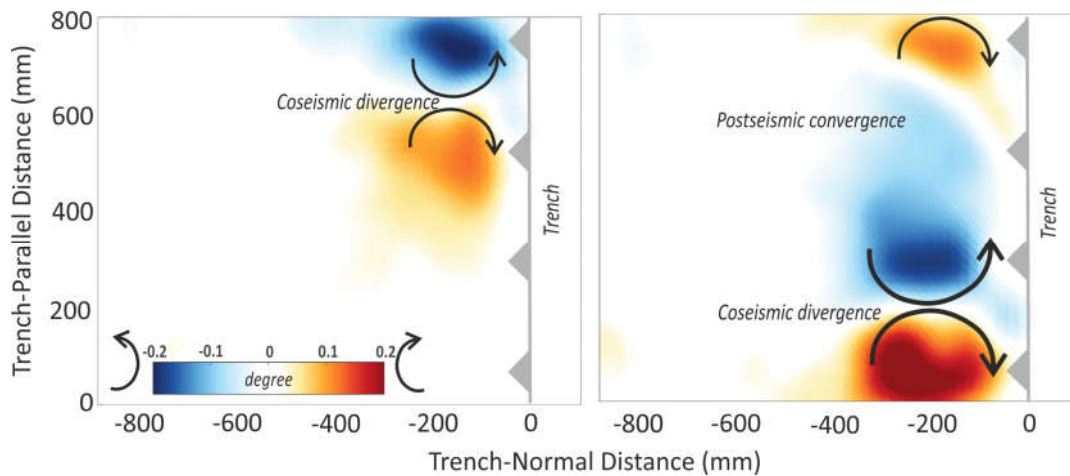
441 We combine kinematic and dynamic results from above to shed light on the mechanism active
442 during an analog earthquake. We analyze and interpret the cumulative displacement fields of a few
443 earthquake cycles for both configurations to reach an accurate view of the elastic responses from
444 the slab and upper plate to the stress drop on the interface (Figure 6 & S4). Starting simple and in
445 line with the *elastic rebound theory* (Reid, 1910), the coseismic strain release (i.e., shear-stress
446 drop) leads to the rebound of the interseismically strained upper plate and slab and transfers stress
447 to the adjacent and nearby regions. The elastic response manifests itself in the strain energy
448 converted to kinetic energy and consumed to accelerate the upper plate and (subordinately) the
449 slab. The rebounds on the upper plate and slab (i.e., opposite sides of the megathrust interface) are
450 in opposite directions (Savage, 1983). When we examine the velocity changes of the plates, we
451 find that the model slab accelerates landward (Figures 6 & S4). The slab velocity increases by
452 50%-300% of the long-term velocity co- and early postseismically, depending on the event’s
453 magnitude. The magnitude of the events and slab accelerations indicate a positive correlation: the

454 larger the earthquake, the stronger is the response generated (Figures 6 & 7). While we cannot
455 measure the elastic rebound of the slab in the asperity area on the interface directly, these values
456 should be considered minimum values of local slab acceleration.

457 4.3 Effect of the slab acceleration on the rapid relocking

458 Our simplified seismotectonic megathrust model suggests different rebounds (i.e., in terms of
459 timing, magnitude, and direction) in the upper plate and slab, triggering the immediate early-
460 postseismic signals. An immediate relocking starts after rupture arrest and leads to a reversed
461 surface displacement. While the rapid relocking is apparently limited on the two MSPs (in the
462 heterogeneous system), it may postseismically reach a significant amount of the coseismic slip
463 increments. The elastic response of the slab (“delayed rebound”), which comes into play as local
464 acceleration, speeds up the stress build-up and results in this accelerated backslip. The large normal
465 faulting aftershocks in the slab following a megathrust event seaward of the megathrust event,
466 such as occurring after the Maule (Ruiz & Contreras-Reyes, 2015) Tohoku-Oki earthquakes

467



468

469 **Figure 8:** Exemplary clockwise and anticlockwise upper plate rotation during coseismic and early
470 postseismic stages derived from selected surface displacements increments. Their associated
471 surface displacements (E07 and E11) are visualized in Figure S2.

472

473 (Asano *et al.*, 2011; Lay *et al.*, 2011) reflect slab extension and thus the same elastic response of
474 the slab.

475 While the acceleration's impact appears as rearward surface displacements above the MSPs, the
476 surface displacements above the matrix follow the slip sense of the MSPs in the heterogeneous
477 configuration (S2). The significant amount of backslip suggests that the delayed rebound may not
478 be the only possible mechanism involved in the rearward surface displacement. An extreme
479 coseismic stress-drop overshoots the strained upper plate trenchward coseismically. The upper
480 plate postseismically responds to this overshoot such that its elastic restoring force drags it back
481 to a quasi-equilibrium state, which may appear as localized upper plate rearward surface
482 displacements to a quasi-equilibrium state (Figure 9).

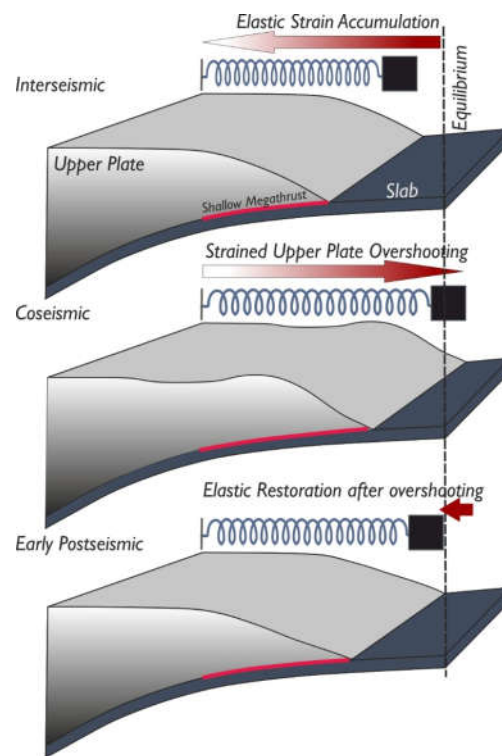
483 An immediate relocking and a high backslip velocity have been modeled based on land-limited
484 GPS stations for the 2007 Pisco (Remy et al., 2016) and the 2010 Maule (Bedford et al., 2016)
485 megathrust earthquakes, respectively. In the Tohoku-Oki earthquake region, the sparse sites
486 directly above the high-slip zone postseismically moved landward faster than the pre-earthquake
487 velocity (Tomita et al., 2015). This fast postseismic velocity has been explained via a slab
488 acceleration driven by the recovery of force balance (Heki & Mitsui, 2013; Yuzariyadi & Heki,
489 2021) and the mantle relaxation (Sun et al., 2014; Watanabe et al., 2014). But it is expected that
490 the mantle relaxation affects surface velocities at a relatively large wavelength. Also, the
491 viscoelastic relaxation could not explain the trenchward motion of the stations above the slip zone
492 further landward from the trench (Yuzariyadi & Heki, 2021). Afterslip might be the responsible
493 mechanism for this surface displacement contrast at a relatively short distance (e.g., Sun & Wang,
494 2015; Tomita et al., 2017). Nevertheless, the coarse sampling rate of near-source observations
495 prevents monitoring how the signals appear and evolve. Our analog model supports the occurrence
496 of significant postseismic velocity changes with the slab deceleration following Omori-Utsu's
497 decay law (Figure S4) of aftershock activity (Utsu et al., 1995). However, any viscoelastic behavior
498 of the mantle may modify the elastic response of the slab and lead to a different response time
499 scale. It means that the acceleration may last longer postseismically and decay with another
500 characteristic time-constant in a coupled brittle-viscous system.

501 The stress evolution model for the extreme weakening observed during the Tohoku-Oki
502 earthquake suggests a 20% slip reversal in the rupture's final stage, consistent with the postseismic
503 stress stage derived from breakout data (Brodsky et al., 2017, 2020). However, our models suggest
504 that the localized slip reversal may reflect the early postseismic stage due to a slab acceleration
505 and/or a rapid restoration of the upper plate after experiencing elastic overshooting. Moreover, a

506 dynamic slip reversal has been reported in the 2011 Mw 9.0 Tohoku-Oki earthquake by Ide et al
507 (2011). It has been suggested that the reversal of rupture propagation direction (from updip to
508 downdip) and amplified upper plate displacement is caused by coseismic dynamic overshooting,
509 which is consistent with our experimental observation. If the mechanisms of these observations in
510 our experiment and the case of Tohoku-Oki earthquake are compatible, the normal mechanism
511 aftershocks on the interface close to the maximum slip area (Ide et al., 2011; Yagi & Fukahata,
512 2011) may be comparable to our proposed early postseismic backslip.

513 4.4 Effects of the acceleration on the upper plate fault activity

514 Apart from the consequences on the asperities, the accelerated relocking also affects upper-plate
515 shortening and upper-plate fault activity. The antithetic fault in our experiments switches its
516 kinematic mode and acts as a normal fault coseismically due to its location relative to the
517 megathrust earthquake centroid (e.g., deDontney et al., 2012; Li et al., 2014; Xu et al., 2015). This
518 discontinuity inside the upper plate responds to stress perturbation and stress enhancement. When
519 the MSPs are in opposite modes in the heterogeneous system (loading vs. unloading), they cause
520 compressional (postseismically) and extensional (coseismically and/or early postseismically)
521 stress regimes on the two segments of the antithetic upper plate fault, respectively. The high
522 amount of the early postseismic shortening (Figure S5; postseismic/interseismic=20-25%) may
523 increase the stress level in the upper plate, which is consistent with the reported upper-plate
524 seismicity after megathrust earthquakes (e.g., Asano et al., 2011; Hoskins et al., 2021; Toda et al.,
525 2011).



526

527 **Figure 9.** Schematic diagram of upper plate elastic behavior during coseismic overshooting and
 528 postseismic restoration. The interseismically strained upper plate is overshoot trenchward
 529 (seaward) due to an extreme coseismic stress-drop on the interface. Subsequently, an elastic
 530 restoring force drags the upper plate back to its equilibrium state.

531

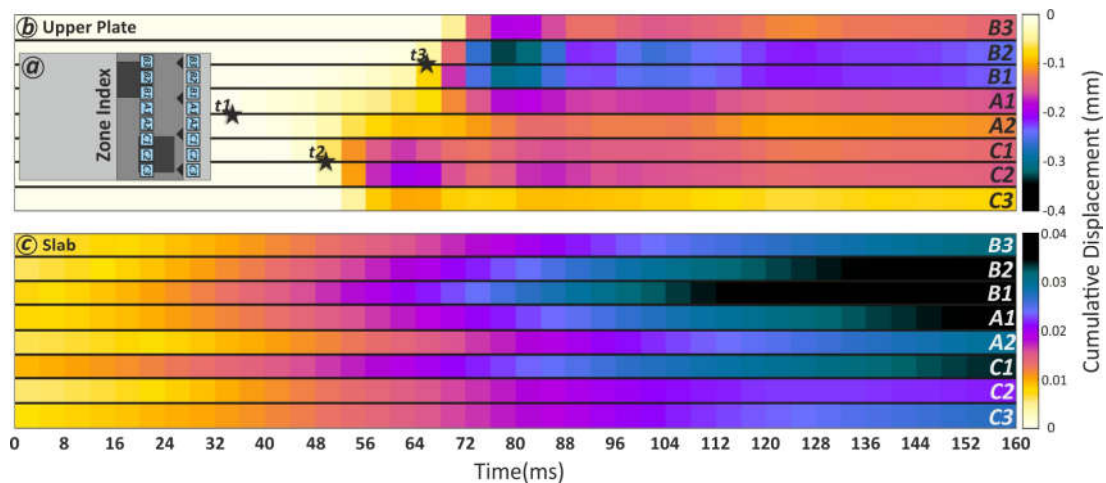
532 4.5 Effects of the acceleration on event triggering

533 The early-postseismic Δ CFS enhancement in the slab may increase the tensional load in the slab
 534 (e.g., Lay *et al.*, 1989; Tilmann *et al.*, 2016) such that the postseismic extensional domain hosts
 535 the large normal mechanism aftershocks early after the megathrust event (e.g., Asano *et al.*, 2011;
 536 Lay *et al.*, 2011; Ruiz and Contreras-Reyes, 2015). The stress enhancement on either receiver MSP
 537 (direct effect) or subducting plate (indirect effect) may bring the second MSP close to failure. In
 538 the heterogeneous configuration, the stress drop of the former event enhances Δ CFS on the second
 539 MSP, such that it directly increases the probability of failure. On the other hand, comparing the
 540 timing of slab acceleration and the latter event (t_2 versus t_3) shows that the acceleration occurs
 541 ahead of the later event. This interestingly suggests that the acceleration caused by the delayed

542 elastic response of the slab has antedated the later event on the shallow MSP (Figures 10 & S6).
543 Hence, the acceleration perturbs the MSP's seismic cycle and causes a “clock advance” in the
544 loading cycle of the MSP (Figures S6 and S7).

545 The rupture of one asperity enhances the stress changes on the adjacent asperity and may bring it
546 closer to failure. For example, Melnick *et al.* (2017) suggest that, besides static stress changes, the
547 increased locking appears in segments adjacent to the failed asperity due to a combination of
548 viscoelastic mantle relaxation and afterslip-controlled vertical axis rotation in the upper plate. The
549 studies on the Wenchuan-Lushan sequential events on the Longmenshan fault show accelerated
550 healing on an asperity in response to an earthquake on the adjacent asperity (Pei *et al.*, 2019; Zhao
551 *et al.*, 2020). Accordingly, the enhanced postseismic compression and the accelerating
552 accumulation of the elastic strain triggered the second event on the nearby asperity (Li *et al.*, 2018).

553



554

555

556 **Figure 10.** Timing of coseismic and postseismic elastic responses of the upper plate and slab for
557 a representative event. a: relative location of the time-series on both plates shown as zone index;
558 b: the elastic response of the upper-plate. t_1 to t_3 indicates the relative timing of the events; c: the
559 elastic response of the slab.

560

561

562

563

564

565 5. Summary and conclusion

566 An earthquake-induced stress drop on a megathrust is related to different responses on the upper
567 plate and slab. In an attempt to monitor and document these observations, we established two
568 generic seismotectonic scale models to mimic homogeneous and heterogenous subduction
569 megathrust (i.e., shallow interface) to generate analog earthquakes. The submillimeter surface
570 displacement during rupture propagation and early-postseismic period is captured by high
571 resolution (temporally and spatially) laboratory seismogeodetic method.

572 Our result shows a sequential elastic rebound following the coseismic shear-stress drop in our
573 elastic-frictional models as the rebound of the upper plate is faster and more prominent compared
574 to that of the slab. The delayed rebound of the slab, along with rapid relaxation of the upper plate
575 after an elastic overshooting, may accelerate the relocking of the megathrust. The laboratory
576 seismogeodetic observations show how the upper plate responds to this overshoot postseismically
577 such that the elastic restoring force may appear as localized upper plate rearward surface
578 displacements. This acceleration triggers/antedates the failure of a nearby asperity and enhances
579 the early backslip in the rupture area. However, depending on the scaling factors, this sequence of
580 dynamic overshooting, amplified motion of the upper plate, and upper plate rearward restoration
581 may alternatively be considered as the coseismic phase. We suggest that the immediate backslip
582 following the main event on the patches could reach up to 30% of coseismic and the entire
583 interseismic backslip. The slip models of the upper plate fault demonstrate that the different
584 segments of the upper plate backthrust may move in opposite directions (normal versus reverse),
585 reflecting the sense of shear on the MSPs (slip versus backslip). This deep-rooted backthrust fault
586 generates a discontinuity in the upper plate and perturbs the inner-wedge stress state.
587 Consequently, the discontinuity may highly enhance the Δ CFS in the upper plate.

588

589 **Acknowledgment**

590 All data in this study will be published open access soon (data archiving is underway). We thank
591 GFZ Data Services for publishing the data. Meanwhile, the data set is uploaded as Supplemental
592 Material 2 for review purposes. The research is supported by the SUBITOP Marie Skłodowska-
593 Curie Action project from the European Union's EU Framework Programme for Research and
594 Innovation Horizon 2020 (Grant Agreement 674899) and partially funded by Deutsche

595 Forschungsgemeinschaft (DFG) through Grant CRC 1114 “Scaling Cascades in Complex
596 Systems,” Project 235221301, Project (B01). The authors thank M. Rudolf and F. Neumann for
597 their helpful discussion and assistance during our laboratory experiments.

598
599

600 **References**

- 601 Adam, J., Urai, J. L., Wieneke, B., Oncken, O., Pfeiffer, K., Kukowski, N., Lohrmann, J., Hoth,
602 S., Van Der Zee, W., & Schmatz, J. (2005). Shear localisation and strain distribution during
603 tectonic faulting—New insights from granular-flow experiments and high-resolution optical
604 image correlation techniques. *Journal of Structural Geology*, *27*(2), 283–301.
- 605 Allmendinger, R. W., Reilinger, R., & Loveless, J. (2007). Strain and rotation rate from GPS in
606 Tibet, Anatolia, and the Altiplano. *Tectonics*, *26*(3). <https://doi.org/10.1029/2006TC002030>
- 607 Ammon, C. J., Ji, C., Thio, H. K., Robinson, D., Ni, S., Hjorleifsdottir, V., Kanamori, H., Lay,
608 T., Das, S., Helmberger, D., Ichinose, G., Polet, J., & Wald, D. (2005). Rupture process of
609 the 2004 Sumatra-Andaman earthquake. *Science*, *308*(5725), 1133–1139.
610 https://doi.org/10.1126/SCIENCE.1112260/SUPPL_FILE/AMMON.SOM.PDF
- 611 Asano, Y., Saito, T., Ito, Y., Shiomi, K., Hirose, H., Matsumoto, T., Aoi, S., Hori, S., &
612 Sekiguchi, S. (2011). Spatial distribution and focal mechanisms of aftershocks of the 2011
613 off the Pacific coast of Tohoku Earthquake. *Earth, Planets and Space*, *63*(7), 669–673.
614 <https://doi.org/10.5047/eps.2011.06.016>
- 615 Bedford, J., Moreno, M., Baez, J. C., Lange, D., Tilmann, F., Rosenau, M., Heidbach, O.,
616 Oncken, O., Bartsch, M., Rietbrock, A., Tassara, A., Bevis, M., & Vigny, C. (2013). A
617 high-resolution, time-variable afterslip model for the 2010 Maule Mw = 8.8, Chile
618 megathrust earthquake. *Earth and Planetary Science Letters*, *383*, 26–36.
619 <https://doi.org/10.1016/j.epsl.2013.09.020>
- 620 Bedford, J., Moreno, M., Li, S., Oncken, O., Baez, J. C., Bevis, M., Heidbach, O., & Lange, D.
621 (2016). Separating rapid relocking, afterslip, and viscoelastic relaxation: An application of
622 the postseismic straightening method to the Maule 2010 cGPS. *Journal of Geophysical
623 Research: Solid Earth*, *121*(10), 7618–7638. <https://doi.org/10.1002/2016JB013093>
- 624 Bedford, J. R., Moreno, M., Deng, Z., Oncken, O., Schurr, B., John, T., Báez, J. C., & Bevis, M.
625 (2020). Months-long thousand-kilometre-scale wobbling before great subduction
626 earthquakes. *Nature* *2020* *580*:7805, *580*(7805), 628–635. [https://doi.org/10.1038/s41586-
627 020-2212-1](https://doi.org/10.1038/s41586-020-2212-1)
- 628 Bilek, S. L., & Lay, T. (2002). Tsunami earthquakes possibly widespread manifestations of
629 frictional conditional stability. *Geophysical Research Letters*, *29*(14), 18–1.
630 <https://doi.org/10.1029/2002GL015215>
- 631 Brodsky, E. E., Mori, J. J., Anderson, L., Chester, F. M., Conin, M., Dunham, E. M., Eguchi, N.,
632 Fulton, P. M., Hino, R., Hirose, T., Ikari, M. J., Ishikawa, T., Jeppson, T., Kano, Y.,
633 Kirkpatrick, J., Kodaira, S., Lin, W., Nakamura, Y., Rabinowitz, H. S., ... Yang, T. (2020).
634 The State of Stress on the Fault Before, During, and After a Major Earthquake. *Annual
635 Review of Earth and Planetary Sciences*, *48*(1), 49–74. [https://doi.org/10.1146/annurev-
636 earth-053018-060507](https://doi.org/10.1146/annurev-earth-053018-060507)
- 637 Brodsky, E. E., Saffer, D., Fulton, P., Chester, F., Conin, M., Huffman, K., Moore, J. C., & Wu,
638 H.-Y. (2017). The postearthquake stress state on the Tohoku megathrust as constrained by
639 reanalysis of the JFAST breakout data. *Geophysical Research Letters*, *44*(16), 8294–8302.

640 <https://doi.org/10.1002/2017GL074027>

641 Caniven, Y., & Dominguez, S. (2021). Validation of a Multilayered Analog Model Integrating
642 Crust-Mantle Visco-Elastic Coupling to Investigate Subduction Megathrust Earthquake
643 Cycle. *Journal of Geophysical Research: Solid Earth*, 126(2), e2020JB020342.
644 <https://doi.org/10.1029/2020JB020342>

645 Chaves, E. J., Schwartz, S. Y., & Abercrombie, R. E. (2020). Repeating earthquakes record fault
646 weakening and healing in areas of megathrust postseismic slip. *Science Advances*, 6(32),
647 eaaz9317. <https://doi.org/10.1126/sciadv.aaz9317>

648 Chlieh, M., Avouac, J. P., Sieh, K., Natawidjaja, D. H., & Galetzka, J. (2008). Heterogeneous
649 coupling of the Sumatran megathrust constrained by geodetic and paleogeodetic
650 measurements. *Journal of Geophysical Research: Solid Earth*, 113, 5305.
651 <https://doi.org/10.1029/2007JB004981>

652 Corbi, F., Sandri, L., Bedford, J., Funicello, F., Brizzi, S., Rosenau, M., & Lallemand, S. (2019).
653 Machine Learning Can Predict the Timing and Size of Analog Earthquakes. *Geophysical*
654 *Research Letters*, 46(3), 1303–1311. <https://doi.org/10.1029/2018GL081251>

655 Corbi, Fabio, Bedford, J., Sandri, L., Funicello, F., Gualandi, A., & Rosenau, M. (2020).
656 Predicting imminence of analog megathrust earthquakes with Machine Learning:
657 Implications for monitoring subduction zones. *Geophysical Research Letters*, 47(7),
658 e2019GL086615. <https://doi.org/10.1029/2019GL086615>

659 Corbi, Fabio, Herrendörfer, R., Funicello, F., & van Dinther, Y. (2017). Controls of seismogenic
660 zone width and subduction velocity on interplate seismicity: Insights from analog and
661 numerical models. *Geophysical Research Letters*, 44(12), 6082–6091.
662 <https://doi.org/10.1002/2016GL072415>

663 deDontney, N., Rice, J. R., & Dmowska, R. (2012). Finite element modeling of branched
664 ruptures including off-fault plasticity. *Bulletin of the Seismological Society of America*,
665 102(2), 541–562. <https://doi.org/10.1785/0120110134>

666 Gao, X., & Wang, K. (2017). Rheological separation of the megathrust seismogenic zone and
667 episodic tremor and slip. *Nature 2017 543:7645*, 543(7645), 416–419.
668 <https://doi.org/10.1038/nature21389>

669 Heki, K., & Mitsui, Y. (2013). Accelerated pacific plate subduction following interplate thrust
670 earthquakes at the Japan trench. *Earth and Planetary Science Letters*, 363, 44–49.
671 <https://doi.org/10.1016/j.epsl.2012.12.031>

672 Hicks, S. P., & Rietbrock, A. (2015). Seismic slip on an upper-plate normal fault during a large
673 subduction megathrust rupture. *Nature Geoscience*, 8(12), 955–960.
674 <https://doi.org/10.1038/ngeo2585>

675 Hoffmann, F., Metzger, S., Moreno, M., Deng, Z., Sippl, C., Ortega-Culaciati, F., & Oncken, O.
676 (2018). Characterizing Afterslip and Ground Displacement Rate Increase Following the
677 2014 Iquique-Pisagua Mw 8.1 Earthquake, Northern Chile. *Journal of Geophysical*
678 *Research: Solid Earth*, 123(5), 4171–4192. <https://doi.org/10.1002/2017JB014970>

679 Hoskins, M. C., Meltzer, A., Font, Y., Agurto-Detzel, H., Vaca, S., Rolandone, F., Nocquet, J.
680 M., Soto-Cordero, L., Stachnik, J. C., Beck, S., Lynner, C., Ruiz, M., Alvarado, A.,
681 Hernandez, S., Charvis, P., Regnier, M., Leon-Rios, S., & Rietbrock, A. (2021). Triggered
682 crustal earthquake swarm across subduction segment boundary after the 2016 Pedernales,
683 Ecuador megathrust earthquake. *Earth and Planetary Science Letters*, 553, 116620.
684 <https://doi.org/10.1016/j.epsl.2020.116620>

685 Hsu, Y. J., Simons, M., Avouac, J. P., Galetzka, J., Sieh, K., Chlieh, M., Natawidjaja, D.,

- 686 Prawirodirdjo, L., & Bock, Y. (2006). Frictional afterslip following the 2005 Nias-Simeulue
687 earthquake, Sumatra. *Science*, *312*(5782), 1921–1926.
688 <https://doi.org/10.1126/science.1126960>
- 689 Ide, S., Baltay, A., & Beroza, G. C. (2011). Shallow dynamic overshoot and energetic deep
690 rupture in the 2011 Mw 9.0 Tohoku-Oki earthquake. *Science*, *332*(6036), 1426–1429.
691 <https://doi.org/10.1126/science.1207020>
- 692 Im, K., & Avouac, J. P. (2021). Tectonic tremor as friction-induced inertial vibration. *Earth and
693 Planetary Science Letters*, *576*, 117238. <https://doi.org/10.1016/J.EPSL.2021.117238>
- 694 Im, K., Marone, C., & Elsworth, D. (2019). The transition from steady frictional sliding to
695 inertia-dominated instability with rate and state friction. *Journal of the Mechanics and
696 Physics of Solids*, *122*, 116–125. <https://doi.org/10.1016/J.JMPS.2018.08.026>
- 697 Kato, A., Sakai, S., & Obara, K. (2011). A normal-faulting seismic sequence triggered by the
698 2011 off the Pacific coast of Tohoku Earthquake: Wholesale stress regime changes in the
699 upper plate. *Earth, Planets and Space*, *63*(7), 745–748.
700 <https://doi.org/10.5047/eps.2011.06.014>
- 701 King Hubbert, M. (1937). Theory of scale models as applied to the study of geologic structures.
702 *Bulletin of the Geological Society of America*, *48*(10), 1459–1520.
703 <https://doi.org/10.1130/GSAB-48-1459>
- 704 Kosari, E., Rosenau, M., Bedford, J., Rudolf, M., & Oncken, O. (2020). On the Relationship
705 Between Offshore Geodetic Coverage and Slip Model Uncertainty: Analog Megathrust
706 Earthquake Case Studies. *Geophysical Research Letters*, *47*(15).
707 <https://doi.org/10.1029/2020GL088266>
- 708 Lay, T., Ammon, C. J., Kanamori, H., Kim, M. J., & Xue, L. (2011). Outer trench-slope faulting
709 and the 2011 Mw 9.0 off the Pacific coast of Tohoku Earthquake. *Earth, Planets and Space*,
710 *63*(7), 713–718. <https://doi.org/10.5047/eps.2011.05.006>
- 711 Lay, T., Astiz, L., Kanamori, H., & Christensen, D. H. (1989). Temporal variation of large
712 intraplate earthquakes in coupled subduction zones. *Physics of the Earth and Planetary
713 Interiors*, *54*(3–4), 258–312. [https://doi.org/10.1016/0031-9201\(89\)90247-1](https://doi.org/10.1016/0031-9201(89)90247-1)
- 714 Lay, T., Kanamori, H., Ammon, C. J., Nettles, M., Ward, S. N., Aster, R. C., Beck, S. L., Bilek,
715 S. L., Brudzinski, M. R., Butler, R., Deshon, H. R., Ekström, G., Satake, K., & Sipkin, S.
716 (2005). The great Sumatra-Andaman earthquake of 26 December 2004. *Science*, *308*(5725),
717 1127–1133. https://doi.org/10.1126/SCIENCE.1112250/SUPPL_FILE/LAY_SOM.PDF
- 718 Li, S., Moreno, M., Bedford, J., Rosenau, M., & Oncken, O. (2015). Revisiting viscoelastic
719 effects on interseismic deformation and locking degree: A case study of the Peru-North
720 Chile subduction zone. *Journal of Geophysical Research: Solid Earth*, *120*(6), 4522–4538.
721 <https://doi.org/10.1002/2015JB011903>
- 722 Li, S., Moreno, M., Rosenau, M., Melnick, D., & Oncken, O. (2014). Splay fault triggering by
723 great subduction earthquakes inferred from finite element models. *Geophysical Research
724 Letters*, *41*(2), 385–391. <https://doi.org/10.1002/2013GL058598>
- 725 Li, Y., Zhang, G., Shan, X., Liu, Y., Wu, Y., Liang, H., Qu, C., & Song, X. (2018). GPS-Derived
726 Fault Coupling of the Longmenshan Fault Associated with the 2008 Mw Wenchuan 7.9
727 Earthquake and Its Tectonic Implications. *Remote Sensing*, *10*(5), 753.
728 <https://doi.org/10.3390/rs10050753>
- 729 Lin, J., & Stein, R. S. (2004). Stress triggering in thrust and subduction earthquakes and stress
730 interaction between the southern San Andreas and nearby thrust and strike-slip faults.
731 *Journal of Geophysical Research: Solid Earth*, *109*(B2).

732 <https://doi.org/10.1029/2003jb002607>
733 Loveless, J. P. (2017). Super-interseismic periods: Redefining earthquake recurrence. In
734 *Geophysical Research Letters* (Vol. 44, Issue 3, pp. 1329–1332). Blackwell Publishing Ltd.
735 <https://doi.org/10.1002/2017GL072525>
736 Loveless, J. P., & Meade, B. J. (2011). Spatial correlation of interseismic coupling and coseismic
737 rupture extent of the 2011 MW = 9.0 Tohoku-oki earthquake. *Geophysical Research*
738 *Letters*, 38(17), 17306. <https://doi.org/10.1029/2011GL048561>
739 Materna, K., Bartlow, N., Wech, A., Williams, C., & Bürgmann, R. (2019). Dynamically
740 Triggered Changes of Plate Interface Coupling in Southern Cascadia. *Geophysical Research*
741 *Letters*, 46(22), 12890–12899. <https://doi.org/10.1029/2019GL084395>
742 Melnick, D., Moreno, M., Quinteros, J., Baez, J. C., Deng, Z., Li, S., & Oncken, O. (2017). The
743 super-interseismic phase of the megathrust earthquake cycle in Chile. *Geophysical*
744 *Research Letters*, 44(2), 784–791. <https://doi.org/10.1002/2016GL071845>
745 Moreno, M., Rosenau, M., & Oncken, O. (2010). 2010 Maule earthquake slip correlates with
746 pre-seismic locking of Andean subduction zone. *Nature* 2010 467:7312, 467(7312), 198–
747 202. <https://doi.org/10.1038/nature09349>
748 Pei, S., Niu, F., Ben-Zion, Y., Sun, Q., Liu, Y., Xue, X., Su, J., & Shao, Z. (2019). Seismic
749 velocity reduction and accelerated recovery due to earthquakes on the Longmenshan fault.
750 *Nature Geoscience*, 12(5), 387–392.
751 Ramberg, H. (1967). Model Experimentation of the Effect of Gravity on Tectonic Processes.
752 *Geophysical Journal International*, 14(1–4), 307–329. [https://doi.org/10.1111/J.1365-](https://doi.org/10.1111/J.1365-246X.1967.TB06247.X)
753 [246X.1967.TB06247.X](https://doi.org/10.1111/J.1365-246X.1967.TB06247.X)
754 Reid, H. F. (1910). The mechanism of the earthquake, the california earthquake of April 18,
755 1906, Report of the state earthquake investigation commission. In *Washington DC:*
756 *Carnegie Institution* (Vol. 2).
757 Remy, D., Perfettini, H., Cotte, N., Avouac, J. P., Chlieh, M., Bondoux, F., Sladen, A., Tavera,
758 H., & Socquet, A. (2016). Postseismic relocking of the subduction megathrust following the
759 2007 Pisco, Peru, earthquake. *Journal of Geophysical Research: Solid Earth*, 121(5), 3978–
760 3995. <https://doi.org/10.1002/2015JB012417>
761 Rice, J. R. (1993). Spatio-temporal complexity of slip on a fault. *Journal of Geophysical*
762 *Research: Solid Earth*, 98(B6), 9885–9907. <https://doi.org/10.1029/93JB00191>
763 Rice, J. R., & Ruina, A. L. (1983). Stability of Steady Frictional Slipping. *Journal of Applied*
764 *Mechanics*, 50(2), 343–349. <https://doi.org/10.1115/1.3167042>
765 Rice, J. R., & Tse, S. T. (1986). Dynamic motion of a single degree of freedom system following
766 a rate and state dependent friction law. *Journal of Geophysical Research: Solid Earth*,
767 91(B1), 521–530. <https://doi.org/10.1029/JB091IB01P00521>
768 Rosenau, M., Corbi, F., & Dominguez, S. (2017). *Analogue earthquakes and seismic cycles:*
769 *experimental modelling across timescales. Solid Earth, European Geosciences Union.* 8(3),
770 597–635. <https://doi.org/10.5194/se-8-597-2017i>
771 Rosenau, M., Horenko, I., Corbi, F., Rudolf, M., Kornhuber, R., & Oncken, O. (2019).
772 Synchronization of Great Subduction Megathrust Earthquakes: Insights From Scale Model
773 Analysis. *Journal of Geophysical Research: Solid Earth*, 124(4), 3646–3661.
774 <https://doi.org/10.1029/2018JB016597>
775 Rosenau, M., Lohrmann, J., & Oncken, O. (2009). Shocks in a box: An analogue model of
776 subduction earthquake cycles with application to seismotectonic forearc evolution. *Journal*
777 *of Geophysical Research: Solid Earth*, 114(B1), 1409.

778 <https://doi.org/10.1029/2008JB005665>

779 Rosenau, M., Nerlich, R., Brune, S., & Oncken, O. (2010). Experimental insights into the scaling
780 and variability of local tsunamis triggered by giant subduction megathrust earthquakes.
781 *Journal of Geophysical Research: Solid Earth*, *115*(9).
782 <https://doi.org/10.1029/2009JB007100>

783 Rosenau, M., & Oncken, O. (2009). Fore-arc deformation controls frequency-size distribution of
784 megathrust earthquakes in subduction zones. *Journal of Geophysical Research*, *114*(B10),
785 B10311. <https://doi.org/10.1029/2009JB006359>

786 Ruff, L. J., & Tichelaar, B. W. (1996). What Controls the Seismogenic Plate Interface in
787 Subduction Zones? *Geophysical Monograph Series*, *96*, 105–111.
788 <https://doi.org/10.1029/GM096P0105>

789 Ruiz, J. A., & Contreras-Reyes, E. (2015). Outer rise seismicity boosted by the Maule 2010 Mw
790 8.8 megathrust earthquake. *Tectonophysics*, *653*, 127–139.
791 <https://doi.org/10.1016/j.tecto.2015.04.007>

792 Savage, J. C. (1983). A dislocation model of strain accumulation and release at a subduction
793 zone. *Journal of Geophysical Research*, *88*(B6), 4984–4996.
794 <https://doi.org/10.1029/JB088iB06p04984>

795 Schmalzle, G. M., McCaffrey, R., & Creager, K. C. (2014). Central Cascadia subduction zone
796 creep. *Geochemistry, Geophysics, Geosystems*, *15*(4), 1515–1532.
797 <https://doi.org/10.1002/2013GC005172>

798 Simons, M., Minson, S. E., Sladen, A., Ortega, F., Jiang, J., Owen, S. E., Meng, L., Ampuero, J.-
799 P., Wei, S., Chu, R., Helmberger, D. V., Kanamori, H., Hetland, E., Moore, A. W., &
800 Webb, F. H. (2011). The 2011 Magnitude 9.0 Tohoku-Oki Earthquake: Mosaicking the
801 Megathrust from Seconds to Centuries. *Science*, *332*(6036), 1421–1425.
802 <https://doi.org/10.1126/SCIENCE.1206731>

803 Sun, T., & Wang, K. (2015). Viscoelastic relaxation following subduction earthquakes and its
804 effects on afterslip determination. *Journal of Geophysical Research: Solid Earth*, *120*(2),
805 1329–1344. <https://doi.org/10.1002/2014JB011707>

806 Sun, T., Wang, K., Iinuma, T., Hino, R., He, J., Fujimoto, H., Kido, M., Osada, Y., Miura, S.,
807 Ohta, Y., & Hu, Y. (2014). Prevalence of viscoelastic relaxation after the 2011 Tohoku-oki
808 earthquake. *Nature*, *514*(7520), 84–87. <https://doi.org/10.1038/nature13778>

809 Tilmann, F., Zhang, Y., Moreno, M., Saul, J., Eckelmann, F., Palo, M., Deng, Z., Babeyko, A.,
810 Chen, K., Baez, J. C., Schurr, B., Wang, R., & Dahm, T. (2016). The 2015 Illapel
811 earthquake, central Chile: A type case for a characteristic earthquake? *Geophysical*
812 *Research Letters*, *43*(2), 574–583. <https://doi.org/10.1002/2015GL066963>

813 Toda, S., Stein, R. S., & Lin, J. (2011). Widespread seismicity excitation throughout central
814 Japan following the 2011 M=9.0 Tohoku earthquake and its interpretation by Coulomb
815 stress transfer. *Geophysical Research Letters*, *38*(7).
816 [https://doi.org/10.1029/2011GL047834@10.1002/\(ISSN\)1944-8007.MEGAQUAKE1](https://doi.org/10.1029/2011GL047834@10.1002/(ISSN)1944-8007.MEGAQUAKE1)

817 Tomita, F., Kido, M., Ohta, Y., Iinuma, T., & Hino, R. (2017). Along-Trench variation in
818 seafloor displacements after the 2011 Tohoku earthquake. *Science Advances*, *3*(7),
819 e1700113. <https://doi.org/10.1126/sciadv.1700113>

820 Tomita, F., Kido, M., Osada, Y., Hino, R., Ohta, Y., & Iinuma, T. (2015). First measurement of
821 the displacement rate of the Pacific Plate near the Japan Trench after the 2011 Tohoku-Oki
822 earthquake using GPS/acoustic technique. *Geophysical Research Letters*, *42*(20), 8391–
823 8397. <https://doi.org/10.1002/2015GL065746>

824 Uchida, N., & Bürgmann, R. (2019). Repeating earthquakes. *Annual Review of Earth and*
825 *Planetary Sciences*, 47(1), 305–332. <https://doi.org/10.1146/annurev-earth-053018-060119>

826 Utsu, T., Ogata, Y., S. R., & Matsu'ura. (1995). The Centenary of the Omori Formula for a
827 Decay Law of Aftershock Activity. *Journal of Physics of the Earth*, 43(1), 1–33.
828 <https://doi.org/10.4294/jpe1952.43.1>

829 Wang, K., Hu, Y., & He, J. (2012). Deformation cycles of subduction earthquakes in a
830 viscoelastic Earth. *Nature*, 484(7394), 327–332. <https://doi.org/10.1038/nature11032>

831 Watanabe, S., Sato, M., Fujita, M., Ishikawa, T., Yokota, Y., Ujihara, N., & Asada, A. (2014).
832 Evidence of viscoelastic deformation following the 2011 Tohoku-Oki earthquake revealed
833 from seafloor geodetic observation. *Geophysical Research Letters*, 41(16), 5789–5796.
834 <https://doi.org/10.1002/2014GL061134>

835 Weiss, J. R., Qiu, Q., Barbot, S., Wright, T. J., Foster, J. H., Saunders, A., Brooks, B. A., Bevis,
836 M., Kendrick, E., Ericksen, T. L., Avery, J., Smalley, R. S., Cimbaro, S. R., Lenzano, L. E.,
837 Barón, J., Báez, J. C., & Echalar, A. (2019). Illuminating subduction zone rheological
838 properties in the wake of a giant earthquake. *Science Advances*, 5(12), 6720–6738.
839 <https://doi.org/10.1126/sciadv.aax6720>

840 Xu, S., Fukuyama, E., Ben-Zion, Y., & Ampuero, J. P. (2015). Dynamic rupture activation of
841 backthrust fault branching. *Tectonophysics*, 644, 161–183.
842 <https://doi.org/10.1016/j.tecto.2015.01.011>

843 Yagi, Y., & Fukahata, Y. (2011). Rupture process of the 2011 Tohoku-oki earthquake and
844 absolute elastic strain release. *Geophysical Research Letters*, 38(19).
845 <https://doi.org/10.1029/2011GL048701>

846 Yuzariyadi, M., & Heki, K. (2021). Enhancement of interplate coupling in adjacent segments
847 after recent megathrust earthquakes. *Tectonophysics*, 801, 228719.
848 <https://doi.org/10.1016/j.tecto.2021.228719>

849 Zhao, J., Ren, J., Liu, J., Jiang, Z., Liu, X., Liang, H., Niu, A., Yue, C., & Yuan, Z. (2020).
850 Coupling fraction and relocking process of the Longmenshan Fault Zone following the 2008
851 Mw7. 9 Wenchuan earthquake. *Journal of Geodynamics*, 101730.

852

853